

The Incident Angle Dependence of CHD₃ Dissociation on the Stepped Pt(211) Surface

Helen Chadwick^{1}, Ana Gutiérrez-González², Davide Migliorini¹, Rainer D. Beck² and Geert-Jan Kroes¹*

1. Leiden Institute of Chemistry, Gorlaeus Laboratories, Leiden University, P.O. Box 9502, 2300 RA Leiden, The Netherlands.
2. Laboratoire de Chimie Physique Moléculaire, Ecole Polytechnique Fédérale de Lausanne, CH-1015 Lausanne, Switzerland.

ABSTRACT

The dissociation of methane on transition metal surfaces is not only of fundamental interest, but also of industrial importance as it represents a rate controlling step in the steam reforming reaction, used commercially to produce hydrogen. Recently, a specific reaction parameter functional (SRP32-vdW) has been developed which describes the dissociative chemisorption of CHD_3 at normal incidence on Ni(111), Pt(111) and Pt(211) within chemical accuracy (4.2 kJ/mol). Here we further test the validity of this functional by comparing the initial sticking coefficients (S_0) obtained from *ab-initio* molecular dynamics calculations run using this functional with those measured with the King and Wells method at different angles of incidence for CHD_3 dissociation on Pt(211). The two sets of data are in good agreement, demonstrating that the SRP32-vdW functional also accurately describes CHD_3 dissociation at off normal angles of incidence. When the direction of incidence is perpendicular to the step edges, an asymmetry is seen in the reactivity with respect to the surface normal, with S_0 being higher when the molecule is directed towards the (100) step rather than the (111) terrace. Whilst there is a small shadowing effect, the trends in S_0 can be attributed to different activation barriers for different surface sites, which in turn is related to the generalized co-ordination numbers of the surface atom to which the dissociating molecule is adsorbed in the transition state. Consequently, most reactivity is seen on the least co-ordinated step atoms at all angles of incidence.

1. Introduction

The dissociation of molecules on stepped and corrugated transition metal surfaces can be considered to model the reaction at defect sites on transition metal catalysts^{1,2}. Calculations have shown that for the dissociation of methane less co-ordinated surface atoms typically have lower activation barriers³⁻⁸, which can influence the dynamics of the collision of the molecule with the surface. For the dissociation of methane on ‘flat’, low index transition metal surfaces, the sticking coefficient, S_0 , typically increases with increasing incident energy due to the significant activation barrier⁹⁻¹⁴, although Utz *et al.* reported an increase in S_0 with decreasing incident energy on Ir(111) which they attributed to precursor mediated dissociation¹⁵. Normal energy scaling, where the reactivity is proportional to the incident translational energy directed normal to the surface, has been seen for methane dissociation on Ni(111)¹⁶, Pt(111)¹⁷ and Pd(111)¹⁸. For the corrugated Pt(110)-(1x2) surface, deviations from normal energy scaling were observed^{19,20}, both for molecules without vibrational energy and for molecules prepared in the antisymmetric stretch overtone state²⁰. When the velocity of the methane was directed parallel to the rows in the Pt(110)-(1x2) surface, normal energy scaling was seen^{19,20}, but when the incident energy was perpendicular to the rows Madix *et al.*¹⁹ reported a scaling of $E_i \cos^{0.5} \theta_i$, where E_i is the incidence energy and θ_i the polar angle of incidence. Bisson *et al.*²⁰ attributed this slower decrease in S_0 to a shadowing effect as at larger values of θ_i the methane preferentially collided with a ridge atom where the activation barrier to the reaction is lowest.

Previous experimental work by Gee *et al.* also reported that S_0 for methane dissociation on stepped Pt(533) does not follow normal energy scaling²¹. They found that the sticking coefficients fell more slowly as the incident methane was directed towards the (100) step than the (111) terrace. By assuming that the reactivity on the (111) terrace is the same as on an

extended Pt(111) surface, they could separate the total sticking coefficient into a contribution from the (100) step and (111) terrace. The authors found that the reactivity on each facet of the surface fell faster than would be predicted by normal energy scaling.

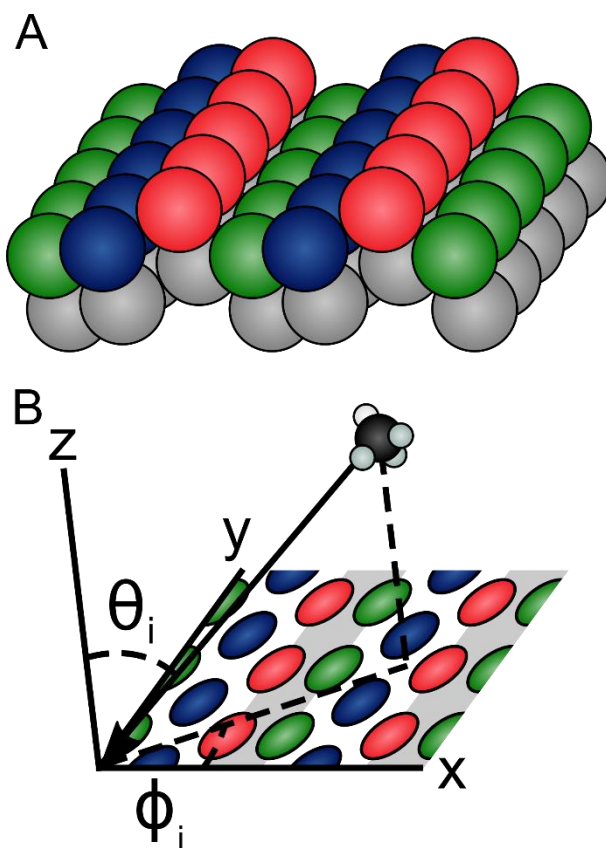


Figure 1. Panel A. Schematic depiction of the Pt(211) surface showing the step (red), terrace (blue) and corner (green) atoms. The three atom wide (111) terraces consist of the green, blue and red atoms, and the one atom high (100) step the adjacent red and green atoms (the shaded area in panel B). The y-axis is parallel to the step edges, the x-axis along the direction of the corrugation and the z-axis perpendicular to the macroscopic (211) plane. Panel B. Depiction of the polar angle θ_i and the azimuthal angle ϕ_i which define the direction of the incoming CHD₃.

In the current work, we present a combined experimental-theoretical study of the dependence of S_0 on the angle of incidence of CHD₃ with respect to a Pt(211) surface. The Pt(211) surface is stepped, consisting of three atom wide (111) terraces separated by one atom

high (100) steps, as shown schematically in Figure 1A. There are three different types of atoms on this surface, which we refer to as step (red), terrace (blue) and corner (green), to be consistent with the notation used in previous studies^{8,22,23}. The (111) terrace consists of the red, blue and green atoms and the (100) step of adjacent red and green atoms, as shown by the shaded area in Figure 1B. The direction of incidence of the molecule is defined by a polar angle, θ_i , and an azimuthal angle, ϕ_i , as also shown in Figure 1B. For $\phi_i = 0^\circ$, changing θ_i corresponds to the molecule being directed towards the (111) terrace ($\theta_i < 0^\circ$) or the (100) step ($\theta_i > 0^\circ$). At $\theta_i \approx -20^\circ$, the molecule's velocity is perpendicular to the (111) terrace and at $\theta_i \approx 40^\circ$ it is perpendicular to the (100) step. The angle $\theta_i = 0^\circ$ corresponds to incidence along the macroscopic surface normal. When $\phi_i = 90^\circ$ changing θ_i changes the component of the velocity parallel to the step edge. Due to the symmetry of the surface, if $\phi_i = 90^\circ$, $|\theta_i|$ and $-|\theta_i|$ correspond to the same incidence condition.

In the calculations, we will make use of the SRP32-vdW specific reaction parameter exchange correlation functional, which was developed to give a chemically accurate (within 4.2 kJ/mol) description of CHD₃ dissociation on Ni(111)²⁴. The same functional has been shown to also reproduce S₀ for CHD₃ dissociation on Pt(111) and Pt(211)⁴ to within chemical accuracy as well as to develop a 15 dimensional neural network potential energy surface for methane dissociation on Ni(111)²⁵. All this previous work with the SRP32-vdW functional has been done with the methane approaching the transition metal surfaces at normal incidence; this presents the first study where the angle of incidence is changed. The results from the *ab-initio* molecular dynamics (AIMD) calculations run with the SRP32-vdW functional will be used to explain the trends in the experimentally determined sticking coefficients.

The rest of the paper is organized as follows. In Sections 2 and 3 the experimental and the theoretical methods employed in the current study will be briefly described. Section 4 presents the results and discussion before Section 5 summarizes our conclusions.

2. Experimental methods

In the current work, we present different sets of experimental data referred to as 2016 and 2018 (A and B). These were done using the same apparatus and methods, but there are differences between the two sets of measurements that will be highlighted below. The experimental apparatus has been described in detail previously^{4,26} and only the most relevant details will be presented here. In brief, the molecular beam/surface science machine consists of a triply differentially pumped molecular beam source attached to an ultrahigh vacuum (UHV) surface science chamber. For the 2016 set of experiments, a 10 mm diameter Pt(211) single crystal surface was held in a tantalum support between two tungsten wires, whereas for the 2018 measurements a 12 mm diameter single crystal surface was mounted directly between the two tungsten wires. In each case, the surface could be heated resistively to over 1100 K and cooled to less than 100 K through thermal contact with a liquid nitrogen reservoir. The temperature was monitored using a K-type thermocouple that was spot welded to the tantalum mount in the 2016 experiments and directly to the Pt(211) crystal in the 2018 experiments. Whilst this may introduce a small difference in surface temperature between the two sets of measurements, the sticking coefficient was found to be the same within error bars at surface temperatures between 500 K and 800 K. Any small difference in the surface temperature due to the different position of the thermocouple will therefore not significantly affect the data presented here.

In both sets of measurements, the surface was mounted on a manipulator that allows the surface to be both translated and rotated, with the step edge direction parallel to the axis of rotation so changing θ_i corresponded to changing the angle of incidence with respect to the (100) steps and the (111) terraces ($\phi_i = 0^\circ$, see Figure 1). During the depositions, the surface was held at a temperature of 650 K using a PID (proportional, integral, differential) controller, and was cleaned between measurements by Ar^+ sputtering and annealing. The surface cleanliness was confirmed by Auger electron spectroscopy.

The molecular beam was formed by expansion of a 1.5% CHD_3 seeded in H_2 gas mix through a 50 μm diameter hole in a stainless steel nozzle and a 2 mm diameter skimmer. The nozzle was resistively heated to 500 K and the resulting velocity determined using time of flight methods, described in detail in Section S1 of the Supporting Information. For the 2016 experiments this gave a normal incident energy of 96.8 kJ/mol and for the 2018 experiments 98.5 kJ/mol. Different sized apertures in a chopper wheel (diameter 2 mm, 1 mm and 0.5 mm) were used to collimate the molecular beam to ensure all the molecules hit the surface for all angles of incidence. (We direct the interested reader to Figure S7 in Ref. 4 for a schematic of the molecular beam path in the machine.)

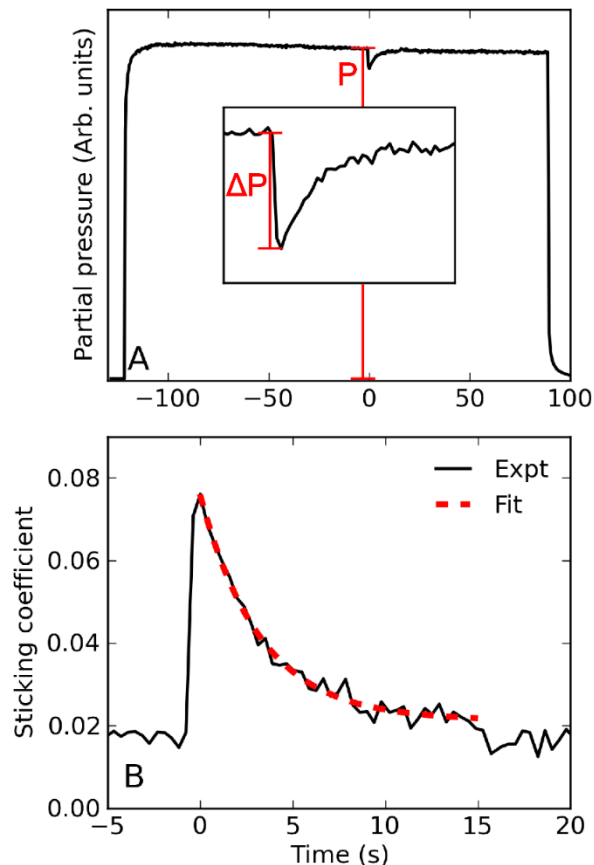


Figure 2. Panel A. King and Wells QMS signal for the dissociative chemisorption of CHD_3 on Pt(211) at a surface temperature of 650 K and an incident energy of 96.8 kJ/mol for $\theta_i = \phi_i = 0^\circ$. The time axis has been shifted so that $t = 0$ s corresponds to the time that the K&W beam flag was opened. The inset shows a magnification of the 15 s that the flag is open for, and the red labels correspond to the quantities in Eq. (1). Panel B. The time dependence of the K&W trace (black) and the fit to the data (dashed red) for the data presented in panel A.

The initial sticking coefficients were determined using the King and Wells (K&W) method^{4,27,28}. An off axis quadrupole mass spectrometer (QMS) was used to monitor the partial pressure of mass 19 in the UHV chamber, with a typical trace presented in Figure 2A. Initially, the separation valve between the molecular beam source and UHV chamber was shut and there is correspondingly no significant mass 19 QMS signal. The separation valve is then opened at $t = -120$ s. At this point, the molecular beam is scattered from an inert beam flag, and the QMS signal is a measure of the total number of molecules entering the UHV chamber. The beam flag

is opened at $t = 0$ s, and the drop in QMS signal corresponds to the number of molecules sticking to the surface. At $t = 15$ s, the beam flag is shut, and the separation valve is shut at $t = 90$ s. The time dependence of the sticking coefficient can then be found using

$$S(t) = \frac{\Delta P(t)}{P} \quad (1)$$

where ΔP is the change in partial pressure when the beam flag is open and P the partial pressure increase when the separation valve is opened. Their values are shown in Figure 2A. $S(t)$ is fit using a double exponential decay²⁸ to obtain the initial sticking coefficient S_0 , as shown in Figure 2B. The baseline of the K&W trace when the flag is shut ($t < 0$ s, $t > 15$ s) is not zero as the QMS current was seen to increase when the beam flag is opened under conditions where no reactivity was observed. This has been accounted for in the analysis of both sets of experimental data and the correction gives rise to the apparent non-zero baseline when the beam flag is closed.

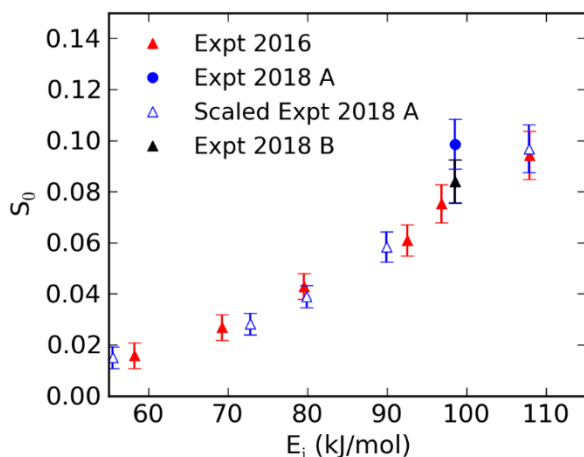


Figure 3. Sticking coefficients obtained from different King and Wells measurements at normal incidence ($\theta_i = 0^\circ$, $\phi_i = 0^\circ$) to the Pt(211) plane at a surface temperature of 650 K. The first experimental data from 2018 (open blue triangles, A) has been scaled to agree with a second data-point at 98.5 kJ/mol (black triangle, B) which are compared to the experiments from 2016⁴ (red). See Section 2 for more details.

We present a comparison of the sticking coefficients measured at normal incidence ($\theta_i = 0^\circ$, $\phi_i = 0^\circ$) at a surface temperature of 650 K from the 2016 (red), 2018 A (blue) and 2018 B (black) experiments in Figure 3. The 2018 A angle of incidence data presented in Section 4 were recorded in the same way as the unscaled 2018 A data shown as a blue filled circle at an incident energy of 98.5 kJ/mol, which is larger than sticking coefficients obtained from the 2016 experiments (the full unscaled data set is shown in the Supporting Information in Figure S5). After the data were recorded, a systematic error was found in the angular 2018 A data due to an unstable backing pressure in the molecular beam expansion. Once this was rectified, the data-point at 98.5 kJ/mol was repeated and the sticking coefficient that was obtained (black, 2018 B) is in agreement with the original 2016 data set. Rescaling the 2018 A data set so that the 98.5 kJ/mol S_0 coincides with the 2018 B data point produced the open symbols in Figure 3, which are in agreement with the 2016 experiments. We therefore chose to rescale the 2018 A angle of incidence data set to bring it into agreement with the 2016 data set at $\theta_i = 0^\circ$, $\phi_i = 0^\circ$. This scaling then accounts for the systematic error in the acquisition of the 2018 A data, and the slightly different normal incident energies obtained at the 500 K nozzle temperature which was used to record the two sets of data. As will be shown in Section 4, this brings the two sets of experiments into excellent agreement for $\theta_i > 0^\circ$, $\phi_i = 0^\circ$ which were recorded in both 2016 and 2018.

3. Theoretical methods

The methods used in the calculations have also been described in detail previously^{4,29} and so only the most relevant details will be presented here. In brief, either 500 or 1000 quasi-classical AIMD trajectories were run for CHD₃ colliding with Pt(211) for $v_1 = 1$ or laser-off conditions, respectively, using the Vienna *ab-initio* simulation package (VASP) version 5.3.5³⁰⁻

³³. We call the AIMD trajectories quasi-classical because zero point energy was imparted to the vibrational modes of CHD₃. The first Brillouin zone was sampled using a 4x4x1 Γ -centered grid with a cut off energy of 350 eV for the plane wave basis set. Projector augmented wave pseudopotentials^{34,35} have been used to represent the core electrons. The Pt(211) surface has been modelled using a 4 layer (1x3) supercell slab^{4,29} with each slab separated from its first periodic replica by 13 Å of vacuum. To facilitate convergence a 0.1 eV Fermi smearing was used. Extensive tests of the parameters used in the calculations have been performed, the results of which can be found in the Supporting Information of Reference 4.

The specific reaction parameter exchange-correlation functional (SRP32-vdW) used in the present work is defined as

$$\text{SRP32-vdW} = (1 - 0.32)E_X^{PBE} + 0.32E_X^{RPBE} + E_C^{vdW} \quad (2)$$

where E_X^{PBE} and E_X^{RPBE} are respectively the PBE^{36,37} and RPBE³⁸ exchange functionals, and E_C^{vdW} is the van der Waals correlation functional of Dion *et al.*³⁹⁻⁴¹. Previous work⁴ has shown that this weighted average produces chemically accurate results for the dissociation of CHD₃ on Pt(211) under normal incidence conditions.

The initial conditions used for the trajectory calculations were sampled to replicate the molecular beam scattering experiments performed in 2016 with the velocity of the molecules sampled from the experimental time of flight measurements and rotated by ϕ_i and θ_i . For the ‘laser-off’ trajectories, the vibrational populations of the molecules were sampled using a Boltzmann distribution at the 500 K nozzle temperature used to create the molecular beam expansion. Whilst it was not possible to perform state-resolved reactivity experiments as the difference between the reactivity of the laser excited molecules could not be separated from the reactivity of the molecules without vibrational excitation, state-resolved calculations were

performed where all the molecules were prepared with a single quantum of C-H stretch vibration in the $J = 2, K = 1, v_1 = 1$ rovibrational state⁴. The initial positions and velocities of the surface atoms were randomly sampled from calculations run to equilibrate the slab at a surface temperature of 650 K.

At the start of the trajectory, the CHD₃ is positioned 6.5 Å above the surface with x and y chosen to randomly sample all the positions on the Pt(211) slab. As in previous work⁴, the kinetic energy of the molecules was increased by 2 kJ/mol to compensate for the potential energy shift due to the unconverged vacuum space. The trajectories were propagated with a time step of 0.4 fs using the velocity-Verlet algorithm until the CHD₃ either dissociated on the Pt(211) surface, scattered back into the gas phase or was trapped on the Pt(211) surface. The molecule was considered to have reacted if one of the bonds in the molecule was greater than 3 Å, whereas if the center of mass (COM) of the molecule was 6.5 Å away from the surface with the COM velocity directed away from the surface it was considered to have been scattered. If neither outcome was reached within the maximum 1 ps timeframe that the trajectory was propagated for, the molecule was considered to be trapped on the surface.

The sticking coefficients were calculated from the AIMD calculations using

$$S_0 = \frac{N_{\text{react}}}{N_{\text{tot}}} \quad (3)$$

where N_{react} is the number of trajectories that dissociate and N_{tot} is the total number of trajectories. The statistical error bars were found as

$$\sigma = \sqrt{\frac{S_0(1 - S_0)}{N_{\text{tot}}}} \quad (4)$$

and represent 68 % confidence limits. The other probabilities and errors presented in Section 4 are calculated with analogous expressions, unless the probability is 0 or 1, in which case the error is calculated as⁴²

$$\sigma = 1 - 0.32^{1/N_{\text{tot}}} \quad (5)$$

which also represent 68 % confidence limits.

4. Results and Discussion

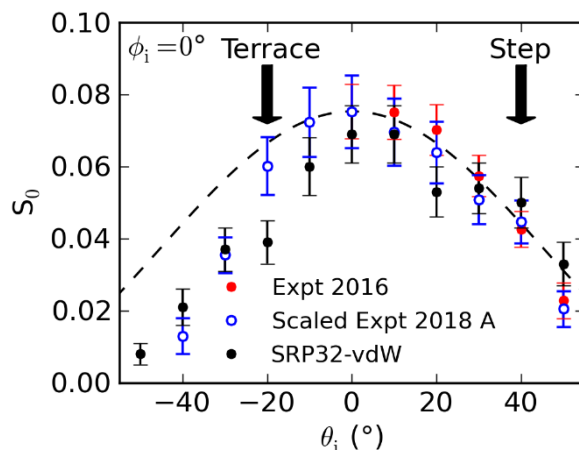


Figure 4. Comparison of the sticking coefficients from the AIMD calculations (black circles) with those from King and Wells experiments at an incident energy of 96.8 kJ/mol (red circles) and scaled sticking coefficients from experiments at an incident energy of 98.5 kJ/mol (blue open circles) for $\phi_i = 0^\circ$. The dashed black line shows a $\cos^2\theta_i$ distribution, and the arrows the angles of incidence perpendicular to the (100) step and the (111) terrace.

Figure 4 presents a comparison of S_0 measured experimentally for $\phi_i = 0^\circ$, $\theta_i \geq 0^\circ$ (red circles) and for $\phi_i = 0^\circ$ for both positive and negative θ_i (open blue circles) with those from AIMD calculations (black). The AIMD calculations were done sampling the velocity distribution used in the 2016 experiments (red) and the 2018 A experimental data (blue) has been scaled to agree with this set of data at $\theta_i = 0^\circ$ (see Section 2). We note that the agreement between the two

sets of experimental data is excellent at $\theta_i > 0^\circ$, further justifying the scaling of the 2018 A data. There is good agreement between the experimental and calculated sticking coefficients, with the value only being significantly different at $\theta_i = -20^\circ$, which we attribute to statistics. The good agreement noted is additional proof of the accuracy of the SRP32-vdW density functional for CHD_3 dissociation on Pt(211) as it seems to give a correct description of the angular dependence of the sticking probability. The dashed line shows $S_0(0^\circ)\cos^2\theta_i$, the incident angle dependence expected for normal energy scaling on a flat surface¹⁶⁻¹⁸, which highlights the asymmetry of S_0 with θ_i seen in both the calculated and experimental sticking coefficients. In both cases, S_0 is seen to drop more quickly as the angle of incidence is changed from normal incidence to towards the (111) terrace (towards negative θ_i) compared to normal incidence to towards the (100) step (positive θ_i) as has been reported previously for methane dissociation on Pt(533)²¹. Furthermore, the sticking coefficients are seen to follow normal energy scaling for $\theta_i > 0^\circ$, but not for $\theta_i < 0^\circ$.

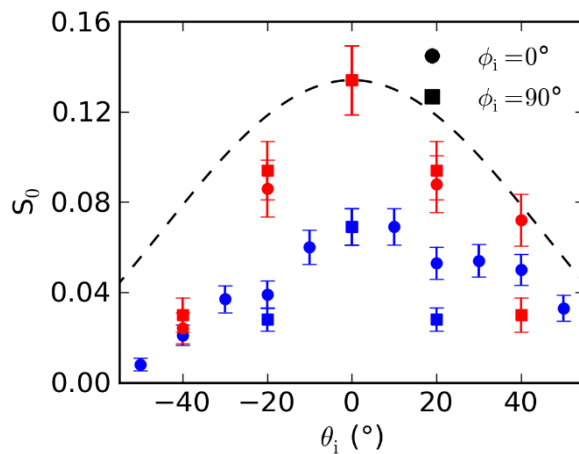


Figure 5. The sticking coefficients obtained from the AIMD calculations for molecules prepared in the $\nu_1 = 1$, $J = 2$ and $K = 1$ rovibrational state (red) and under laser-off conditions (blue) for $\phi_i = 0^\circ$ (circles) and $\phi_i = 90^\circ$ (squares). The dashed black line shows a $\cos^2\theta_i$ distribution for the $\nu_1 = 1$, $\phi_i = 90^\circ$ data (red squares).

Whilst no experimental data is available for $\phi_i = 90^\circ$, AIMD calculations were run with the results (squares) compared with those for $\phi_i = 0^\circ$ (circles) in Figure 5. The sticking coefficients fall as quickly with θ_i for $\phi_i = 90^\circ$ as is seen to occur rotating towards the (111) terrace ($\theta_i < 0^\circ$) for $\phi_i = 0^\circ$ for molecules both under laser-off conditions (blue) and prepared in the $v_1 = 1$, $J = 2$ and $K = 1$ rovibrational state (red). This suggests that for angles where the molecules collide with the (111) terrace only the polar angle of incidence (θ_i) appears to be important, and not the azimuthal angle (ϕ_i). The dashed black line in Figure 5 shows $S_0(0^\circ)\cos^2\theta_i$ scaled to the $v_1 = 1$, $\theta_i = 0^\circ$, $\phi_i = 90^\circ$ sticking coefficient, illustrating that for $\phi_i = 90^\circ$ the reactivity drops more quickly than would be predicted by normal energy scaling. This is in contrast to the Pt(110)-(1x2) surface where the reactivity was found to obey normal energy scaling when the molecules were directed parallel to the ridge atoms²⁰.

Figure 6 shows the position of the center of mass of the molecules at the point where the dissociating bond becomes longer than the transition state value for C-H cleavage (red) and C-D cleavage (blue) for a range of θ_i for $\phi_i = 0^\circ$ for the laser-off trajectories (left column) and for $v_1 = 1$ (right column). The dashed lines in each plot indicate the direction that the CHD₃ approaches the surface. As the angle of incidence changes from normal to the (111) terrace ($\theta_i \approx -20^\circ$) to normal to the (100) step ($\theta_i \approx 40^\circ$) the reaction site shifts from the terrace and step atoms towards the (100) step, reflecting the change in position on the surface where the normal incidence energy is highest. Most of the reactivity is seen to occur on top of the step atoms which is the site with the lowest activation barrier for the dissociation of methane on Pt(211)^{4,8}.

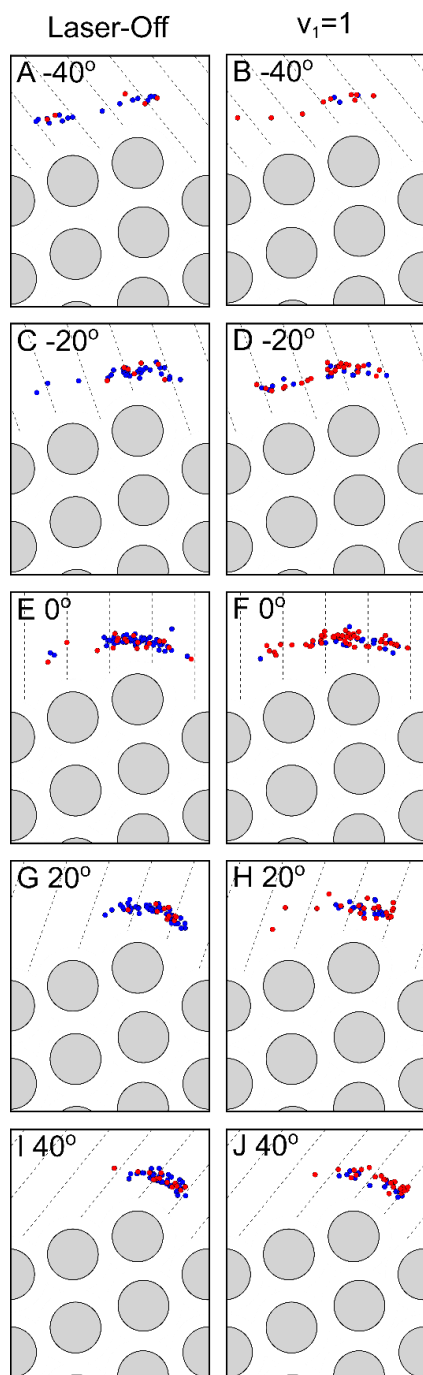


Figure 6. xz plots showing the positions of the center of mass for C-H dissociation (red) and C-D dissociation (blue) under laser-off conditions (left column) and for the $v_1 = 1$ trajectories (right column) for the values of θ_i shown in the top left corner of the plots for $\phi_i = 0^\circ$. The dashed lines show the incident direction of the CHD_3 .

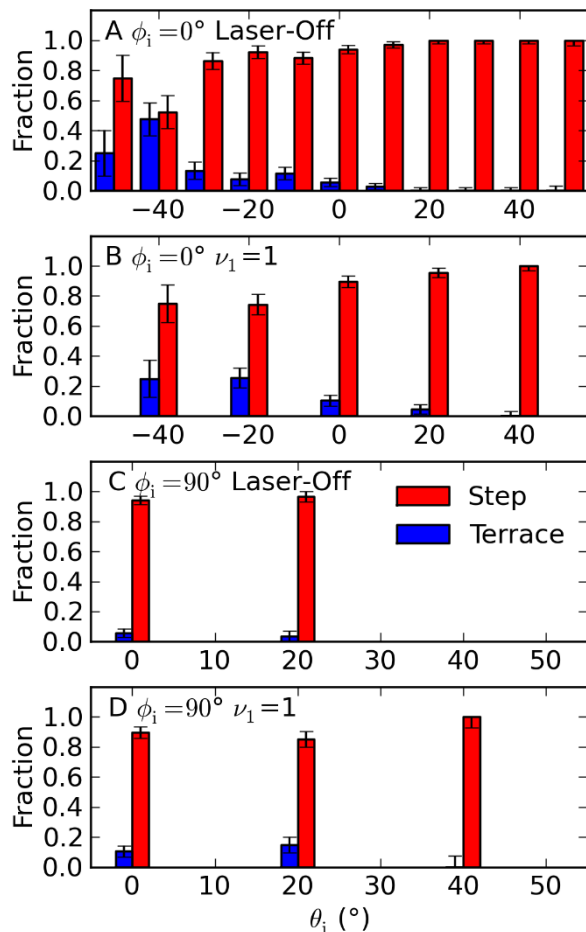


Figure 7. The fraction of molecules that dissociate on the step atoms (red) and on the terrace atoms (blue) calculated for the laser-off (panels A and C) and $\nu_1 = 1$ (panels B and D) trajectories for $\phi_i = 0^\circ$ (panels A and B) and $\phi_i = 90^\circ$ (panels C and D). No dissociation was observed on the corner atoms.

The fraction of molecules that dissociate on the step (red) and terrace (blue) atoms in the AIMD calculations are presented in Figure 7 for $\phi_i = 0^\circ$ (panels A and B) and for $\phi_i = 90^\circ$ (panels C and D) under laser-off conditions (panels A and C) and for molecules prepared with a quantum of C-H stretch vibration (panels B and D). The site of reaction was taken to be the surface atom closest to the center of mass of the CHD_3 when the dissociating bond became larger than the transition state value. It should be noted that no dissociation was seen on the corner atoms at any angle of incidence. Dissociation on the step atoms dominates the reactivity at all angles of

incidence under both laser-off conditions and for $\nu_1 = 1$ which is consistent with previous work at lower incident energies and a surface temperature of 120 K for CH_4 dissociation on Pt(211) at $\theta_i = \phi_i = 0^\circ$ ⁸. The highest reactivity observed on the terrace atoms is seen for $\theta_i < 0^\circ$ at $\phi_i = 0^\circ$, which could be due to the kinetic energy of the incoming molecule normal to the (111) terrace being higher, and the probability of the molecule hitting the terrace atoms being larger.

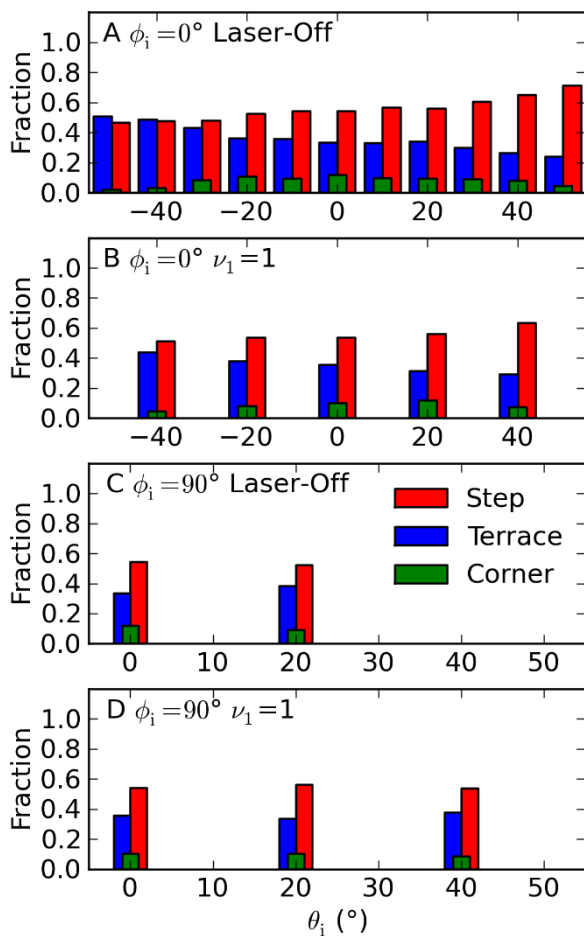


Figure 8. The fraction of all the trajectories that impact nearest the step (red), terrace (blue) and corner (green) atoms for the laser-off (panels A and C) and $\nu_1 = 1$ (panels B and D) calculations for $\phi_i = 0^\circ$ (panels A and B) and $\phi_i = 90^\circ$ (panels C and D).

To decide whether the differences in reactivity at the different angles of incidence can be attributed to a shadowing effect, we identified the surface atom closest to the site of methane impact for both reactive and nonreactive trajectories. The results are shown in Figure 8 for the step (red), terrace (blue) and corner (green) atoms for $\phi_i = 0^\circ$ (panels A and B) and $\phi_i = 90^\circ$ (panels C and D), for the trajectories run sampling laser-off conditions (panels A and C) and for $v_1 = 1$ (panels B and D). At nearly all θ_i most trajectories collide with the more exposed step atoms, and very few hit the corner atoms, where no reactivity is seen (see Figure 7). Figure 8 shows that for $\phi_i = 0^\circ$, with increasing θ_i the number of terrace impacts changes compared to the step impacts from roughly equal for $\theta_i = -50^\circ$ to less than half for $\theta_i = +50^\circ$, indicating a shadowing effect for the terrace sites caused by the step atoms with increasing θ_i (see also Figure 6). There is no significant difference in this shadowing effect for molecules that are initially prepared in $v_1 = 1$ or under laser-off conditions. Note that even for $\theta_i = -20^\circ$ and $\phi_i = 0^\circ$ (incidence perpendicular to the terrace) more molecules hit the step atoms than the terrace atoms.

In order to disentangle the reactivity on each site of the surface from the shadowing effect, we calculated site specific sticking coefficients for each site as

$$S_0(\text{site}) = \frac{N_{\text{react}}(\text{site})}{N_{\text{near}}(\text{site})} \quad (6)$$

where $N_{\text{react}}(\text{site})$ is the number of reactive trajectories for step or terrace atoms, and $N_{\text{near}}(\text{site})$ is the number of trajectories for which that site is the site of impact. $S_0(\text{site})$ are presented in Figure 9 for the step (red) and terrace (blue) sites for $\phi_i = 0^\circ$ (panels A and B) and $\phi_i = 90^\circ$ (panels C and D) for laser-off conditions (panels A and C) and for $v_1 = 1$ (panels B and D). The site specific sticking coefficients are higher for the step atoms than the terrace atoms at all incident angles, with reactivity on the terrace atoms being at its highest when the normal incidence energy to the (111) terrace is higher. This is particularly apparent for the $v_1 = 1$ data

for $\phi_i = 0^\circ$ in Figure 9B where the site specific reaction probability on the terrace atoms is at its maximum at $\theta_i = -20^\circ$, which corresponds to the direction of incidence being normal to the (111) terrace. The same is not seen in the laser-off sticking coefficients in Figure 9A but as the total reactivity is lower the statistics are less good in this analysis. An asymmetry is seen in the reactivity around the angle where $S_0(\text{site})$ is largest for both the step and terrace atoms for $\phi_i = 0^\circ$. This asymmetry cannot be due to shadowing and is therefore likely to be due to different activation barriers for the dissociation at different positions on the Pt(211) surface.

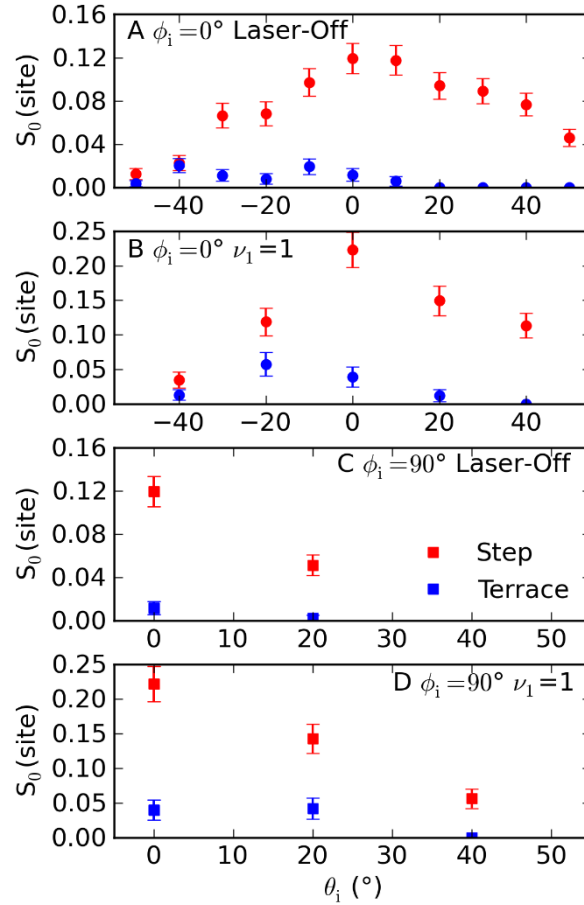


Figure 9. A comparison of the site specific sticking coefficients for each site calculated using Eq. (6) for dissociation on the step atoms (red) and terrace atoms (blue) for the laser-off (panels A and C) and $\nu_1 = 1$ (panels B and D) trajectories for $\phi_i = 0^\circ$ (panels A and B) and $\phi_i = 90^\circ$ (panels C and D).

Activation barriers are typically found to scale linearly with adsorption energies for the dissociation of molecules on transition metal surfaces⁴³⁻⁴⁵. In turn, Calle-Vallejo *et al.* have shown that adsorption energies tend to scale linearly with the generalized co-ordination number of the surface atom to which the molecule adsorbs^{46,47}, which, unlike co-ordination numbers, also takes into account the co-ordination number of the nearest neighbours of the atom of interest. It follows that activation barriers would be expected to scale linearly with the generalized co-ordination number. On Pt(211), the generalized co-ordination number for the step atoms (5.58)⁴⁶ < terrace atoms (7.33) < corner atoms (8.75)⁴⁶, with the activation barriers following the same trend⁸. This would predict most reactivity would occur on the step atoms and least on the corner atoms, as is observed in the AIMD calculations presented here, at all angles of incidence. It is also interesting to note that all the atoms in the Pt(211) surface have a different generalized co-ordination number to those on an extended Pt(111) surface (7.50)⁴⁶ and Pt(100) surface (6.67)⁴⁶ despite the Pt(211) surface consisting of one atom high (100) steps and three atom wide (111) terraces. Previous work by Gee *et al.* has suggested that the dissociation of methane on a Pt(533) surface, which consists of one atom high (100) steps and four atom wide (111) terraces, can be accounted for by considering the Pt(533) surface as independent (100) and (111) facets²¹. As detailed in Section S4 of the Supporting Information, we followed their analysis for the laser-off $\phi_i = 0^\circ$ AIMD calculations for CHD₃ dissociation on Pt(211) and obtained similar qualitative results. However, the description is unlikely to be quantitatively correct, as there are a large number of adjustable parameters in the model, and to obtain good agreement between the model and the AIMD calculations it is necessary to use unphysical values of the angles of the (100) step and the (111) terrace with respect to the (211) plane. This suggests that the structure of Pt(211) should not be considered as consisting of independent (100) and (111) facets for methane

dissociation, as Juurlink *et al.* have previously shown is the case for the dissociation of H₂, O₂ and H₂O on Pt(211)⁴⁸. This is reflected in the differences in the generalized co-ordination numbers of the atoms in the Pt(211), Pt(111) and Pt(100) surfaces.

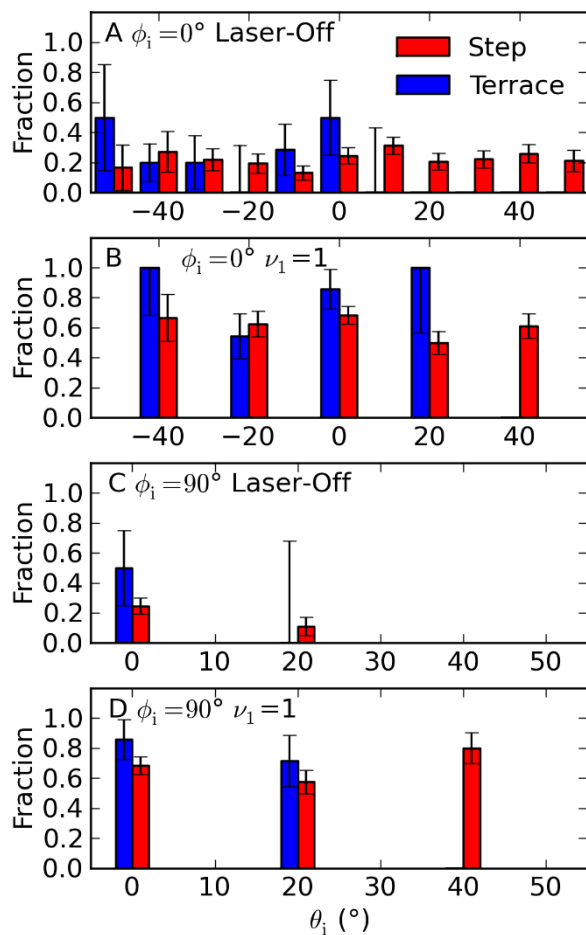


Figure 10. A comparison of the fraction of C-H cleavage calculated for dissociation on the step atoms (red) and terrace atoms (blue) for the laser-off (panels A and C) and $\nu_1 = 1$ (panels B and D) trajectories for $\phi_i = 0^\circ$ (panels A and B) and $\phi_i = 90^\circ$ (panels C and D).

The fraction of C-H cleavage seen in the AIMD calculations is presented in Figure 10 for dissociation on the step (red) and terrace (blue) atoms for $\phi_i = 0^\circ$ (panels A and B) and $\phi_i = 90^\circ$ (panels C and D) for laser-off conditions (panels A and C) and for $\nu_1 = 1$ (panels B and D). For

the laser-off trajectories, the fraction of C-H cleavage is found to be 0.25 for both sites within error bars, as would be expected for a statistical 3:1 branching ratio for C-D:C-H cleavage. More C-H bond cleavage is seen for the $v_1 = 1$ trajectories, with a slightly higher degree of bond-selectivity being observed for dissociation on the terrace atoms than on the step atoms at all angles of incidence, although this difference is within the error bars of the calculations for individual incidence conditions. At a surface temperature of 150 K and at lower incident energies, the branching ratio for the dissociation of CHD_3 , CH_2D_2 and CH_3D on Pt(111) has been shown to be statistical under laser-off conditions⁴⁹ whereas when a quantum of C-H stretch was added to the molecule, only C-H cleavage was observed^{49,50}. Increasing the surface temperature (to 650 K) lowers the effective activation barrier to the dissociative chemisorption due to the thermal motion of the atoms in the surface^{14,51,52}, which combined with a higher incident translational energy is likely to make CHD_3 dissociation less bond selective for $v_1 = 1$, as is seen to be the case in the AIMD calculations.

5. Summary

Sticking coefficients have been measured and calculated for CHD_3 dissociation on a Pt(211) surface at a temperature of 650 K for different angles of incidence at a fixed incident energy (≈ 97 kJ/mol). The measured sticking coefficients, obtained by the King and Wells method, are in good agreement with those from *ab-initio* molecular dynamics calculations using the SRP32-vdW functional, further demonstrating the quality of the functional for describing methane dissociation on Pt(211). An asymmetry is seen in the polar incident angle distribution in both the calculated and the experimental sticking coefficients, with a more rapid drop in reactivity for incidence towards the (111) terraces compared to towards the (100) steps. At all

incident angles, the calculations show that preparing the CHD_3 with one quantum of C-H stretch vibration increases the reactivity and favors C-H bond cleavage over C-D bond cleavage. A shadowing effect is seen which favors impact on the step sites compared to the terrace sites as the polar angle of incidence is increased towards normal incidence to the steps, although this by itself does not account for the difference in reactivity seen at the two sites. The reactivity on the terrace atoms is seen to be highest at angles of incidence where the energy normal to the (111) terrace is highest, but reactivity on the step atoms dominates at all angles of incidence where the activation barrier for dissociation is lowest. The site of the dissociation is seen to shift around the step atoms as the angle of incidence is changed, reflecting the change of position where the normal energy is highest and the difference in activation barrier heights at the different sites of the Pt(211) surface.

ASSOCIATED CONTENT

Supporting Information

Determination of the experimental velocity distribution, comparison of different sets of experimental data, contribution of trapped trajectories to reaction and Pt(211) as a Pt[3(111)x(100)] surface.

ACKNOWLEDGMENTS

This work was supported financially by the Swiss National Science Foundation (grant Nos. P300P2-171247 and 159689/1), the Ecole Polytechnique Fédérale de Lausanne and the

European Research Council through an ERC2013 advanced grant (No. 338580) and with computer time granted by NWO-EW through a Dutch Computing Challenge Project grant.

AUTHOR INFORMATION

Corresponding author

Email: h.j.chadwick@lic.leidenuniv.nl

REFERENCES

- (1) Wolcott, C. A.; Medford, A. J.; Studt, F.; Campbell, C. T. Degree of Rate Control Approach to Computational Catalyst Screening. *J. Catal.* **2015**, *330*, 197–207.
- (2) Xu, Y.; Lausche, A. C.; Wang, S.; Khan, T. S.; Abild-Pedersen, F.; Studt, F.; Nørskov, J. K.; Bligaard, T. *In Silico* Search for Novel Methane Steam Reforming Catalysts. *New J. Phys.* **2013**, *15*, 125021.
- (3) Nave, S.; Tiwari, A. K.; Jackson, B. Methane Dissociation and Adsorption on Ni(111), Pt(111), Ni(100), Pt(100), and Pt(110)-(1×2): Energetic Study. *J. Chem. Phys.* **2010**, *132*, 054705.
- (4) Migliorini, D.; Chadwick, H.; Nattino, F.; Gutiérrez-González, A.; Dombrowski, E.; High, E. A.; Guo, H.; Utz, A. L.; Jackson, B.; Beck, R. D.; et al. Surface Reaction Barriometry: Methane Dissociation on Flat and Stepped Transition Metal Surfaces. *J. Phys. Chem. Lett.* **2017**, *8*, 4177–4182.
- (5) Abild-Pedersen, F.; Lytken, O.; Engbæk, J.; Nielsen, G.; Chorkendorff, I.; Nørskov, J. K. Methane Activation on Ni(111): Effects of Poisons and Step Defects. *Surf. Sci.* **2005**, *590*, 127–137.
- (6) Bengaard, H. S.; Nørskov, J. K.; Sehested, J.; Clausen, B. S.; Nielsen, L. P.; Molenbroek, A. M.; Rostrup-Nielsen, J. R. Steam Reforming and Graphite Formation on Ni Catalysts. *J. Catal.* **2002**, *209*, 365–384.
- (7) Van Santen, R. A. Complementary Structure Sensitive and Insensitive Catalytic Relationships. *Acc. Chem. Res.* **2009**, *42*, 57–66.

- (8) Chadwick, H.; Guo, H.; Gutiérrez-González, A.; Menzel, J. P.; Jackson, B.; Beck, R. D. Methane Dissociation on the Steps and Terraces of Pt(211) Resolved by Quantum State and Impact Site. *J. Chem. Phys.* **2018**, *148*, 014701.
- (9) Beck, R. D.; Utz, A. L. In *Dynamics of Gas-Surface Interactions Atomic-level Understanding of Scattering Processes at Surfaces*; Dâiez Muiãno, R., Busnengo, H. F., Eds.; Springer: Berlin, 2013; Vol 50, pp 179–212.
- (10) Juurlink, L. B. F.; Killelea, D. R.; Utz, A. L. State-Resolved Probes of Methane Dissociation Dynamics. *Prog. Surf. Sci.* **2009**, *84*, 69–134.
- (11) Chadwick, H.; Beck, R. D. Quantum State Resolved Gas-Surface Reaction Dynamics Experiments: A Tutorial Review. *Chem. Soc. Rev.* **2016**, *45*, 3576–3594.
- (12) Chadwick, H.; Beck, R. D. Quantum State-Resolved Studies of Chemisorption Reactions. *Annu. Rev. Phys. Chem.* **2017**, *68*, 39–61.
- (13) Jiang, B.; Yang, M.; Xie, D.; Guo, H. Quantum Dynamics of Polyatomic Dissociative Chemisorption on Transition Metal Surfaces: Mode Specificity and Bond Selectivity. *Chem. Soc. Rev.* **2016**, *45*, 3621-3640.
- (14) Nave, S.; Tawari, A. K.; Jackson, B. Dissociative Chemisorption of Methane on Ni and Pt Surfaces: Mode-Specific Chemistry and the Effects of Lattice Motion. *J. Phys. Chem. A* **2014**, *118*, 9615–9631.
- (15) Dombrowski, E.; Peterson, E.; Del Sesto, D.; Utz, A. L. Precursor-Mediated Reactivity of Vibrationally Hot Molecules: Methane Activation on Ir(111). *Catal. Today* **2015**, *244*, 10–18.

- (16) Lee, M. B.; Yang, Q. Y.; Ceyer, S. T. Dynamics of the Activated Dissociative Chemisorption of CH₄ and Implication for the Pressure Gap in Catalysis: A Molecular Beam–High Resolution Electron Energy Loss Study. *J. Chem. Phys.* **1987**, *87*, 2724–2741.
- (17) Luntz, A. C.; Bethune, D. S. Activation of Methane Dissociation on a Pt(111) Surface. *J. Chem. Phys.* **1989**, *90*, 1274–1280.
- (18) Tait, S. L.; Dohnálek, Z.; Campbell, C. T.; Kay, B. D. Methane Adsorption and Dissociation and Oxygen Adsorption and Reaction with CO on Pd Nanoparticles on MgO(100) and on Pd(111). *Surf. Sci.* **2005**, *591*, 90–107.
- (19) McMaster, M. C.; Madix, R. J. Alkane Dissociation Dynamics on Pt(110)–(1×2). *J. Chem. Phys.* **1993**, *98*, 9963–9976.
- (20) Bisson, R.; Sacchi, M.; Beck, R. D. State-Resolved Reactivity of CH₄ on Pt(110)–(1×2): The Role of Surface Orientation and Impact Site. *J. Chem. Phys.* **2010**, *132*, 094702.
- (21) Gee, A. T.; Hayden, B. E.; Mormiche, C.; Kleyn, A. W.; Riedmüller, B. The Dynamics of the Dissociative Adsorption of Methane on Pt(533). *J. Chem. Phys.* **2003**, *118*, 3334–3341.
- (22) Guo, H.; Farjamnia, A.; Jackson, B. Effects of Lattice Motion on Dissociative Chemisorption: Toward a Rigorous Comparison of Theory with Molecular Beam Experiments. *J. Phys. Chem. Lett.* **2016**, *7*, 4576–4584.
- (23) Durukanog-tildelu, S.; Kara, A.; Rahman, T. S. Local Structural and Vibrational Properties of Stepped Surfaces: Cu(211), Cu(511), and Cu(331). *Phys. Rev. B* **1997**, *55*,

- 13894–13903.
- (24) Nattino, F.; Migliorini, D.; Kroes, G. J.; Dombrowski, E.; High, E. A.; Killelea, D. R.; Utz, A. L. Chemically Accurate Simulation of a Polyatomic Molecule-Metal Surface Reaction. *J. Phys. Chem. Lett.* **2016**, *7*, 2402–2406.
- (25) Zhou, X.; Nattino, F.; Zhang, Y.; Chen, J.; Kroes, G. J.; Guo, H.; Jiang, B. Dissociative Chemisorption of Methane on Ni(111) Using a Chemically Accurate Fifteen Dimensional Potential Energy Surface. *Phys. Chem. Chem. Phys.* **2017**, *19*, 30540–30550.
- (26) Chen, L.; Ueta, H.; Bisson, R.; Beck, R. D. Quantum State-Resolved Gas/Surface Reaction Dynamics Probed by Reflection Absorption Infrared Spectroscopy. *Rev. Sci. Instrum.* **2013**, *84*, 053902.
- (27) King, D. A.; Wells, M. G. Reaction Mechanism in Chemisorption Kinetics: Nitrogen on the {100} Plane of Tungsten. *Proc. R. Soc. London, Ser. A* **1974**, *339*, 245–269.
- (28) Chadwick, H.; Gutiérrez-González, A.; Beck, R. D. Quantum State Resolved Molecular Beam Reflectivity Measurements: CH₄ Dissociation on Pt(111). *J. Chem. Phys.* **2016**, *145*, 174707.
- (29) Nattino, F.; Migliorini, D.; Bonfanti, M.; Kroes, G. J. Methane Dissociation on Pt(111): Searching for a Specific Reaction Parameter Density Functional. *J. Chem. Phys.* **2016**, *144*, 044702.
- (30) Kresse, G.; Hafner, J. *Ab Initio* Molecular Dynamics for Liquid Metals. *Phys. Rev. B* **1993**, *47*, 558–561.
- (31) Kresse, G.; Hafner, J. *Ab Initio* Molecular-Dynamics Simulation of the Liquid-Metal–

- Amorphous-Semiconductor Transition in Germanium. *Phys. Rev. B* **1994**, *49*, 14251–14269.
- (32) Kresse, G.; Furthmüller, J. Efficient Iterative Schemes for *Ab Initio* Total-Energy Calculations Using a Plane-Wave Basis Set. *Phys. Rev. B* **1996**, *54*, 11169–11186.
- (33) Kresse, G.; Furthmüller, J. Efficiency of *Ab-Initio* Total Energy Calculations for Metals and Semiconductors Using a Plane-Wave Basis Set. *Comp. Mater. Sci.* **1996**, *6*, 15–50.
- (34) Kresse, G.; Joubert, D. From Ultrasoft Pseudopotentials to the Projector Augmented-Wave Method. *Phys. Rev. B* **1999**, *59*, 1758–1775.
- (35) Blöchl, P. E. Projector Augmented-Wave Method. *Phys. Rev. B* **1994**, *50*, 17953–17979.
- (36) Perdew, J. P.; Burke, K.; Ernzerhof, M. Generalized Gradient Approximation Made Simple [Phys. Rev. Lett. *77*, 3865 (1996)]. *Phys. Rev. Lett.* **1997**, *78*, 1396.
- (37) Perdew, J. P.; Burke, K.; Ernzerhof, M. Generalized Gradient Approximation Made Simple. *Phys. Rev. Lett.* **1996**, *77*, 3865–3868.
- (38) Hammer, B.; Hansen, L. B.; Nørskov, J. K. Improved Adsorption Energetics within Density-Functional Theory Using Revised Perdew-Burke-Ernzerhof Functionals. *Phys. Rev. B* **1999**, *59*, 7413–7421.
- (39) Thonhauser, T.; Cooper, V. R.; Li, S.; Puzder, A.; Hyldgaard, P.; Langreth, D. C. Van Der Waals Density Functional: Self-Consistent Potential and the Nature of the Van Der Waals Bond. *Phys. Rev. B* **2007**, *76*, 125112.
- (40) Dion, M.; Rydberg, H.; Schröder, E.; Langreth, D. C.; Lundqvist, B. I. Van Der Waals

- Density Functional for General Geometries. *Phys. Rev. Lett.* **2004**, *92*, 246401.
- (41) Román-Pérez, G.; Soler, J. M. Efficient Implementation of a Van Der Waals Density Functional: Application to Double-Wall Carbon Nanotubes. *Phys. Rev. Lett.* **2009**, *103*, 096102.
- (42) Louis, T. A. Confidence Intervals for a Binomial Parameter After Observing No Successes. *Am. Stat.* **1981**, *35*, 154.
- (43) Medford, A. J.; Vojvodic, A.; Hummelshøj, J. S.; Voss, J.; Abild-Pedersen, F.; Studt, F.; Bligaard, T.; Nilsson, A.; Nørskov, J. K. From the Sabatier Principle to a Predictive Theory of Transition-Metal Heterogeneous Catalysis. *J. Catal.* **2015**, *328*, 36–42.
- (44) Latimer, A. A.; Kulkarni, A. R.; Aljama, H.; Montoya, J. H.; Yoo, J. S.; Tsai, C.; Abild-Pedersen, F.; Studt, F.; Nørskov, J. K. Understanding Trends in C–H Bond Activation in Heterogeneous Catalysis. *Nat. Mater.* **2017**, *16*, 225–229.
- (45) Wang, S.; Petzold, V.; Tripkovic, V.; Kleis, J.; Howalt, J. G.; Skúlason, E.; Fernández, E. M.; Hvolbæk, B.; Jones, G.; Toftelund, A.; et al. Universal Transition State Scaling Relations for (De)Hydrogenation over Transition Metals. *Phys. Chem. Chem. Phys.* **2011**, *13*, 20760–20765.
- (46) Calle-Vallejo, F.; Martínez, J. I.; García-Lastra, J. M.; Sautet, P.; Loffreda, D. Fast Prediction of Adsorption Properties for Platinum Nanocatalysts with Generalized Coordination Numbers. *Angew. Chemie Int. Edit.* **2014**, *53*, 8316–8319.
- (47) Calle-Vallejo, F.; Tymoczko, J.; Colic, V.; Vu, Q. H.; Pohl, M. D.; Morgenstern, K.; Loffreda, D.; Sautet, P.; Schuhmann, W.; Bandarenka, A. S. Finding Optimal Surface

- Sites on Heterogeneous Catalysts by Counting Nearest Neighbors. *Science* **2015**, *350*, 185–189.
- (48) Badan, C.; Koper, M. T. M.; Juurlink, L. B. F. How Well Does Pt(211) Represent Pt[n(111) × (100)] Surfaces in Adsorption/Desorption? *J. Phys. Chem. C* **2015**, *119*, 13551–13560.
- (49) Chen, L.; Ueta, H.; Bisson, R.; Beck, R. D. Vibrationally Bond-Selected Chemisorption of Methane Isotopologues on Pt(111) Studied by Reflection Absorption Infrared Spectroscopy. *Faraday Discuss.* **2012**, *157*, 285–295.
- (50) Hundt, P. M.; Ueta, H.; van Reijzen, M. E.; Jiang, B.; Guo, H.; Beck, R. D. Bond-Selective and Mode-Specific Dissociation of CH₃D and CH₂D₂ on Pt(111). *J. Phys. Chem. A* **2015**, *119*, 12442–12448.
- (51) Killelea, D. R.; Campbell, V. L.; Shuman, N. S.; Smith, R. R.; Utz, A. L. Surface Temperature Dependence of Methane Activation on Ni(111). *J. Phys. Chem. C* **2009**, *113*, 20618–20622.
- (52) Campbell, V. L.; Chen, N.; Guo, H.; Jackson, B.; Utz, A. L. Substrate Vibrations as Promoters of Chemical Reactivity on Metal Surfaces. *J. Phys. Chem. A* **2015**, *119*, 12434–12441.

TOC Graphic

